Reconfigurable and Scalable Multimode Silicon Photonics Switch for Energy-Efficient Mode-Division-Multiplexing Systems

Rubana Bahar Priti, *Student Member, IEEE*, and Odile Liboiron-Ladouceur, *Senior Member, IEEE*

***Abstract*—A novel integrated scalable multimode switch (SMS) is experimentally demonstrated using tapered multimode-interference-based couplers and Ti/W metal heater phase shifters for mode-division-multiplexing (MDM) silicon photonics switching. The SMS allows path-reconfigurable switching of the first two (TE0 and TE1) or the first three (TE0, TE1, and TE2) transverse electric (TE) modes using the same device achieving footprint efficiency for higher bandwidth density. A proof-of-concept realization of the two-mode switch demonstrates the (de)multiplexing and switching of broadband optical signals over the TE0 and TE1 modes exhibiting −6.5 dB insertion loss (IL) in the bar state and −7.3 dB IL in the cross state at 1550 nm with less than −14 dB crosstalk. Simultaneous switching of two parallel TE modes (TE0+TE1) exhibits less than −7.0 dB IL and −11.9 dB crosstalk at 1550 nm. An aggregated bandwidth of 2 × 10 Gb/s is experimentally achieved while switching between two non-return-to-zero PRBS31 data signals with <9.8 μs switching time and >17.7 dB switching extinction ratio (ER) for individual-mode transmission, and <7.6 μs switching time and >12.0 dB switching ER for dual-mode transmission. The SMS is scalable to switch higher order TE modes with lower energy consumption (up to 63% less) than the single-mode switches indicating its potential application in energy-efficient MDM photonic networks.**

***Index Terms*—Mode-division-multiplexing, optical interconnects, photonics integrated circuits, silicon photonics, waveguide switches.**

I. Introduction

THE escalating demand of bandwidth density and computation speed in large-scale data centers and high-performance computing (HPC) systems enforce ultra-dense integration of several thousands of massively parallel processors in a single server. As the intra-data center IP traffic is rapidly increasing up to the range of zettabyte [1], the growing number of network resources can be constrained by its large carbon footprint. The compound annual growth rate of electricity consumption in data centers is already double the global projection rate, imposing an environmental concern [2]. Data center interconnects, consuming approximately 10% of the overall server power, will face inevitable challenges in power handling capacity due to the big data paradigm shift [3]. To overcome the economic and environmental challenges in power handling capacity of on-chip and chip-to-chip communication, optical interconnects are a viable alternative to the conventional electrical interconnects [4].

Complementary metal oxide semiconductor (CMOS) compatible silicon-on-insulator (SOI) technology offers low cost, low loss, low power and high bandwidth data communication improving the energy per bit performance of data center interconnects [5]. The bandwidth density can be further increased by introducing dense wavelength-division-multiplexing (DWDM) enabling simultaneous transmission of multiple parallel data signals. Although a three wavelength-channel chip-to-chip WDM link with <1.5 pJ/bit is reported in [6], using WDM in ultra-dense short-reach interconnects (<5 cm) increases fabrication cost and system complexities due to the control, tuning and routing of tens to hundreds of optical channels. As WDM needs individual optical source for each wavelength channel, the large power requirement of the lasers significantly increases the overall power consumption diminishing the merit of DWDM [7]. To exploit the energy advantage of silicon photonics integrated circuits (PICs), DWDM should be combined with advanced multiplexing schemes, such as mode-division-multiplexing (MDM). In the SOI PICs, the large difference in the refractive indices (Δ n $\sim$ 2) between the silicon waveguide and the surrounding oxide allows precise control and manipulation of optical eigenmodes employing MDM as a WDM-compatible multiplexing method [8], [9]. As individual data channels propagate over different orthogonal guided modes, one single laser can be used for multiple data channels increasing energy efficiency.

MDM offers greater bandwidth density, higher aggregated channel capacity, and better energy efficiency in chip scale silicon photonics systems [10]. Sending multiple data signals through a single multimode waveguide structure significantly reduces the device footprint leading to better scalability. However, robust to process variation and low-loss photonics devices are a key requirement in MDM systems, as they are more susceptible to inter-modal crosstalk than single-mode PICs [11]. Energy-efficient photonic switching can be leveraged by using MDM based SOI switches enabling high data throughput leading to better aggregated bandwidth [12]. MDM switches have been reported using micro-ring resonators (MRRs) [13], asymmetric directional couplers (ADCs)

Manuscript received December 6, 2018; revised April 15, 2019; accepted June 3, 2019. Date of publication June 10, 2019; date of current version July 22, 2019. This work was supported in part by the Canada Research Chair Program. *(Corresponding author: Rubana Bahar Priti.)*

The authors are with the Department of Electrical and Computer Engineering, McGill University, Montreal, QC H3A0E9, Canada (e-mail: rubana.priti@mail.mcgill.ca; odile@ieee.org).

Color versions of one or more of the figures in this paper are available online at http://ieeexplore.ieee.org.

Digital Object Identifier 10.1109/JLT.2019.2921797

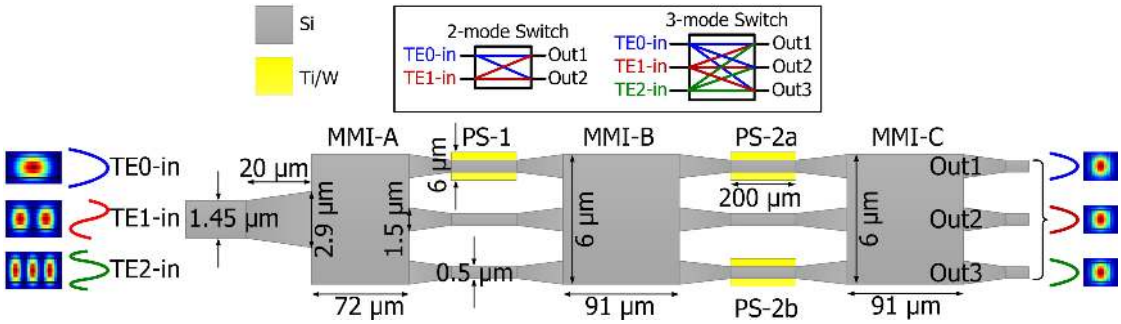

Fig. 1. Schematic of the scalable multimode switch (SMS) with three multimode inputs denoted as *TE0-in*, *TE1-in* and *TE2-in*; and three single-mode outputs, denoted as *Out1*, *Out2* and *Out3*. The block diagrams of a 2-mode switch and a 3-mode switch are shown on top.

[14], Y-branches [15] and multimode interference (MMI) couplers [16].

We recently demonstrate a novel reconfigurable and scalable multimode switch (SMS) using cascaded MMI couplers and titanium/tungsten (Ti/W) metal heater phase shifters operating in the C-band for TE0 and TE1 modes [17]. We recently also report on the experimental demonstration of the SMS for reconfigurable switching of three modes [18]. This work reports on an optimized design of the SMS with improved switching performance, broadband operation and greater scalability for 2-mode transmission. Simultaneous transmission of two parallel data channels over two modes is also experimentally demonstrated. A similar design is reported in [9] consisting of cascaded MMIs and passive waveguide phase shifters for WDM-MDM and WDM-PDM conversion without reconfigurable switching. The SMS offers path-reconfigurable switching of the first three quasi-transverse electric (quasi-TE) modes, i.e., TE0, TE1, and TE2 modes, among three single-mode output ports. As proof-of-concept demonstration, a 2-mode switch for the fundamental and the first order quasi-transverse electric (quasi-TE) modes is experimentally measured using the same structure as the 3-mode switch. The quasi-TE0 and quasi-TE1 modes are launched using only one C-band tunable laser (from 1520 nm to 1580 nm) improving the energy efficiency. The 2-mode SMS exhibits −6.5 dB insertion loss (IL) in bar state and −7.3 dB IL in cross state with a worst-case switching extinction ratio (ER) of 17.7 dB in individual-mode switching. Dynamic switching between two 10 Gb/s nonreturn-to-zero (NRZ) data packets confirms a switching time of less than 9.8 μs with an average heater power of 64.8 mW. Less than −7.0 dB IL and greater than 12.0 dB ER are observed in dual-mode switching. Clear and open eye diagrams are recorded at 10 Gb/s confirming distortion free data transmission with 2 × 10 Gb/s aggregated bandwidth. The scalability analysis estimates a projected −9.0 dB IL and an average 163.0 mW thermal tuning power for a 5-mode switch (i.e. TE0, TE1, TE2, TE3 and TE4) saving up to 63% energy compared to a single-mode switch. The proposed SMS can be potentially used in the high-throughput energy-efficient photonics switching.

II. SMS Design and Working Principle

The schematic of the proposed scalable multimode switch (SMS) is shown in Fig. 1 with simplified block diagrams of a 2-mode switch and a 3-mode switch. The 2-mode switch can switch *TE0-in* and *TE1-in* input modes between *Out1* and *Out2* output ports. In the 3-mode switch, each of the first three TE modes (i.e. TE0, TE1 and TE2) can be switched among three output ports: *Out1*, *Out2* and *Out3*. The SMS consists of three cascaded MMIs (MMI-A, MMI-B and MMI-C) and three metal heater phase shifters (PS-1, PS2a and PS-2b). The waveguide widths for single-mode and multimode propagations are optimized by eigenmode simulation using a commercial CAD tool (Lumerical Mode solution). The widths for TE0, TE1 and TE2 mode propagations are chosen to be 0.5 μm, 1.0 μm and 1.45 μm, respectively, optimized by finite difference eigenmode (FDE) simulation. First three TE modes are multiplexed using a broadband ADC based mode multiplexer, designed following [17]. The multiplexed mixed-mode signal propagates through the multimode waveguide and coupled to the input port of MMI-A, which is a reconfigurable multimode demultiplexer/switch (RMDS); designed using the mechanism of symmetric interference. We proposed and tested this novel silicon photonics component, consisting of a 72 μm long 1 × 3 MMI coupler, in [19] for the (de)multiplexing of two parallel high-speed data channels over two simultaneously transmitted TE modes (TE0+TE1). The input port of the MMI-A has a 2.9 μm wide and 20 μm long taper for the multimode transmission to adiabatically couple TE0, TE1 and TE2 modes to the MMI-A. All I/O ports of the MMI-B and MMI-C have 1.5 μm wide and 20 μm long linear tapers for single-mode transmission. These tapers minimize the optical return losses at each step. The widths of the MMIs are fixed at 6 μm. The lengths of MMI-B and MMI-C are optimized by a fully vectorial and bi-directional eigenmode expansion model, and are chosen to be 91 μm. MMI-B and MMI-C are identically designed with equal widths and lengths, based on the principle of 120° optical hybrid [20]. They form a Mach-Zehnder Interferometer (MZI) enabling reconfigurable switching among the *Out1*, *Out2* and *Out3* single-mode output ports. As MZI based integrated switches need precise control over the power coupling ratios between the coupler's output ports, fabrication tolerant and broadband MMI couplers are a better choice than the ADC and the Y-junction leading to higher extinction ratio (>25 dB) and lower crosstalk [21]. The self-imaging principle of the MMI coupler [22] allows conversion, tuning and low-loss propagation of multiple guided modes using a single set of photonic components reducing footprint and power consumption. The detail design methodology of the MMIs is reported in [16]. Each

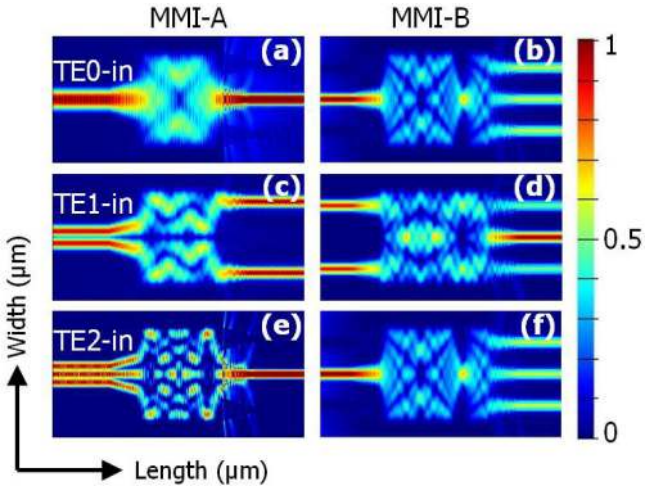

Fig. 2. Simulated electric fields of the MMI-A (left) and MMI-B (right) at 1550 nm. The top (a, b), middle (c, d) and bottom (e, f) images represent the propagation of TE0, TE1 and TE2 modes, respectively.

metal heater phase shifter is 6 μm wide and 200 μm long consisting of 200 nm thick thin film of Ti/W alloy, as shown in Fig. 4(e) of the following section, of 4 Ω/sq sheet resistance.

Fig. 2 shows the simulated electric fields in MMI-A and MMI-B for three input modes. The input TE0 mode (*TE0-in*) is mapped onto the middle output port of MMI-A with a smaller mode field diameter (MFD), as shown in Fig. 2(a), due to the smaller widths of the taper and the waveguide at the output ports. To mitigate the complexities of manipulating different mode orders in the same structure, the higher order TE modes are decomposed to their fundamental components before phase-tuning and propagating through the device. The fundamental components of the *TE1-in* input mode are mapped to the upper and the lower output ports with a π-phase shift (Fig. 2(c)). The TE2 mode input (*TE2-in*) is converted to the fundamental mode with a 66% conversion efficiency, and then mapped to the middle output port of MMI-A (Fig. 2(e)). The reason for the lower conversion efficiency is explained by the odd/even mode-parity [23]. In a 1×3 symmetric interference based MMI, like MMI-A, the input even modes (i.e. TE0 and TE2) reproduce themselves in the middle output port with 100% theoretical efficiency. However, the odd modes (i.e. TE1 and TE3) are converted into lower order modes and equally divided in to the upper and the lower output ports [24], [25]. Thus, the input *TE1-in* mode is divided into TE0 components, as shown in Fig. 2(c). As the input *TE2-in* mode is not converted to its fundamental components in MMI-A's middle output port, phase-tuning of this higher order mode requires a mode insensitive phase shifter which adds complexity to the device and increases the inter-modal crosstalk, hence this scheme is avoided. An additional mode converter efficiently performs the TE2$\rightarrow$ TE0 conversion but, at the same time, filters out the input TE0 mode [26]. A longer device formed by cascaded MMIs and passive phase shifters can potentially improve the conversion efficiency, as proposed in [27], but it significantly increases the device length. Moreover, this device is not capable of mode (de)multiplexing. As a design trade-off, the length of the MMI-A is optimized such that the odd/even parity is discontinued at

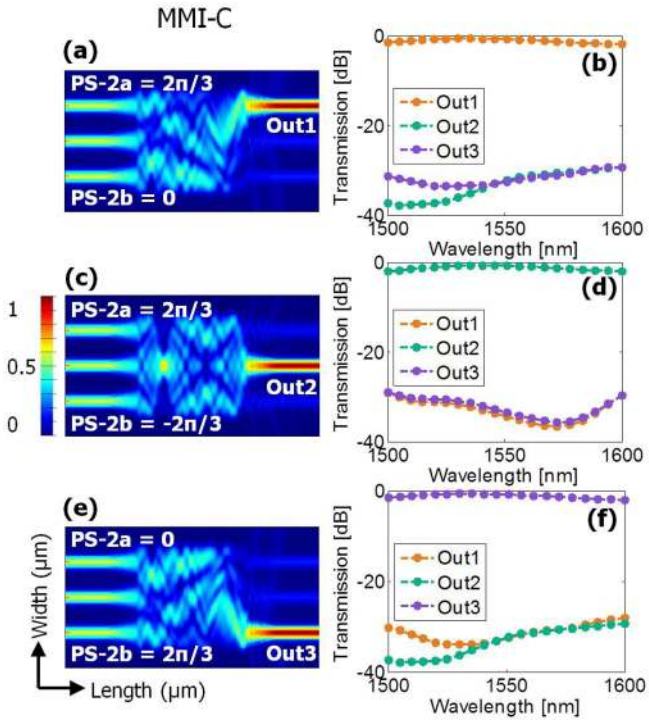

Fig. 3. Simulated electric fields at 1550 nm (left) and calculated optical transmission as a function of wavelength (right) in MMI-C. The top (a, b), middle (c, d), and bottom (e, f) images represent optical transmissions in *Out1*, *Out2* and *Out3* output ports, respectively.

the output end for the *TE2-in* input mode resulting in a lower TE2$\rightarrow$TE0 conversion efficiency at the cost of an increased IL in the switching output ports. A small phase-shift, applied by the PS-1 phase shifter, is required for precise control of the decomposed components of *TE1-in* and *TE2-in* input modes. The fundamental components of *TE0-in*, *TE1-in* and *TE2-in* modes are coupled to the input ports of MMI-B as shown in Fig. 2(b), (d), and (f), respectively. MMI-B, being a 120° optical hybrid, causes a $2\pi/3$ phase difference between each output ports. The incoming light is equally distributed among the output ports of MMI-B for the *TE0-in* and the *TE2-in* modes. The imbalance in power splitting observed in the *TE1-in* mode (Fig. 2(d)) is compensated by the PS-2a and PS-2b phase shifters, which also tune the relative phases of the MMI-B outputs before coupling them onto MMI-C.

The simulated electric fields in MMI-C for switching among *Out1*, *Out2* and *Out3* output ports are shown in Fig. 3(a), (c), and (e), respectively. The corresponding calculated optical transmissions as a function of wavelengths are shown in Fig. 3(b), (d), and (f), respectively. A relative phase-shift of $2\pi/3$ is required between the PS-2a and the PS-2b phase shifters to enable reconfigurable switching. For the *Out1* transmission, the phase-shifts at PS-2a and PS-2b are set to $2\pi/3$ and 0, respectively. When the switching output appears at the *Out2* port, Ps-2a $= 2\pi/3$ and Ps-2b $= -2\pi/3$. Finally, for the *Out3* transmission, the phase-shifts at PS-2a and PS-2b are 0 and $2\pi/3$, respectively. The calculated insertion losses (IL) range between -0.7 dB to -1.8 dB within 1500 nm to 1600 nm wavelength range for all three output ports. The estimated crosstalk is less than -29.0 dB in all cases. The

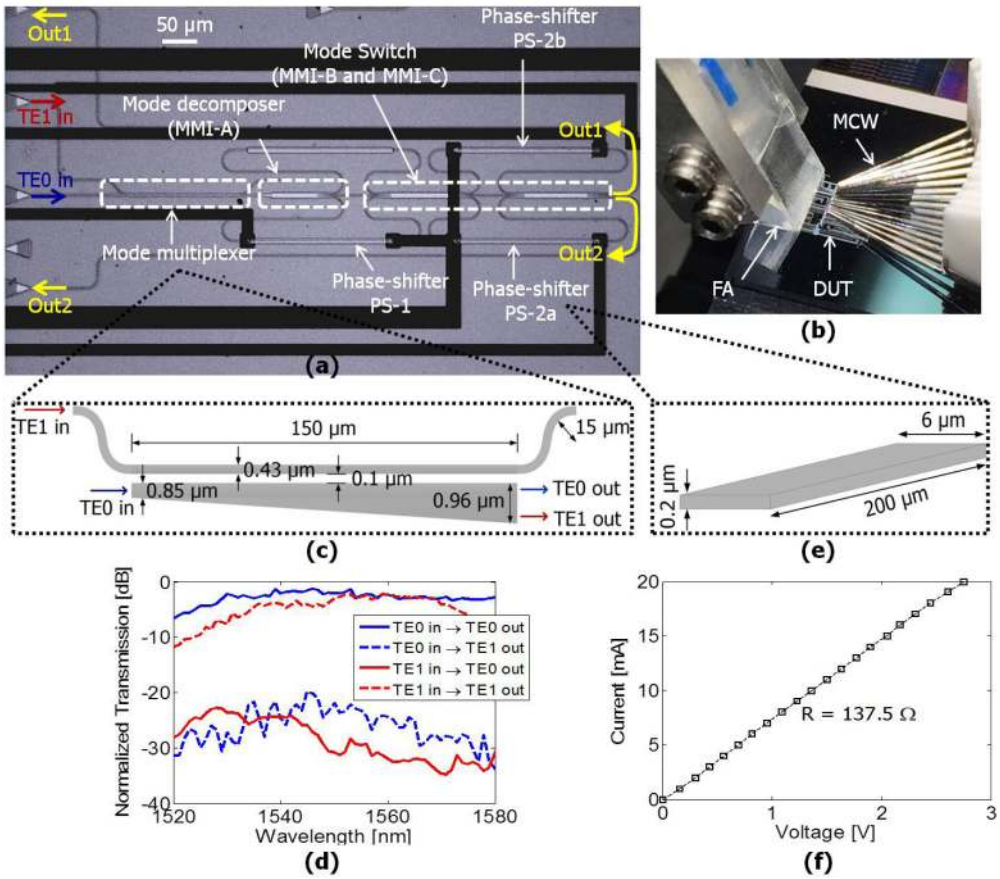

Fig. 4. (a) Optical micrograph of the fabricated chip of the 2-mode SMS. (b) Experimental test bed of the DC measurement showing a vertically coupled 8-fiber array (FA), a 15-pin multi-contact wedge (MCW) DC probe, and the silicon photonics SMS device under test (DUT). (c) Schematic (top view) of the ADC based 2-mode multiplexer. (d) Normalized optical transmission of the 2-mode multiplexer as a function of wavelength. (e) 3D schematic of the Ti/W metal heater phase shifter. (f) Measured current-voltage characteristic curve of the phase shifter.

operation principle of the dual-mode (*TE0+TE1-in*) transmission is reported in [19].

III. SMS Fabrication and Characterization

The SMS is fabricated through Applied Nanotools Inc. using a SOI wafer of 220 nm thick silicon device layer, 2.0 μm buried-oxide (BOX) layer, and 675 μm silicon handle layer [28]. The device is patterned using a 100 keV electron-beam-lithography (EBL), followed by an inductively coupled plasma-induced reactive ion etching (ICP-RIE) process. Then, a 2.2 μm silicon dioxide (SiO_2) is deposited using chemical vapor deposition (CVD) to protect and isolate the silicon device layer. On top of this oxide layer, 200 nm thin film of Ti/W alloy is deposited as high-resistance heater and 300 nm thin film of aluminum is deposited for the electrical routing using electron-beam evaporation. After metallization, a 300 nm SiO_2 layer is deposited as a protective layer for the heaters, which is etched away over the aluminum pads for electrical probing. A subset of the proposed SMS (Fig. 1) enabling reconfigurable switching of TE0 and TE1 modes between two output channels is experimentally measured. Simultaneous 2-mode switching between two parallel high-speed optical signals is also demonstrated. The characterization results of the 3-mode switch (3MS) are reported in [18]. An optical micrograph of the fabricated chip for the 2-mode switch is shown in Fig. 4(a). As the 2-mode switch needs only two output ports, the middle output port of the 3-mode switch (*Out2* in Fig. 1) is tapered down, and the upper and the lower output ports are denoted as *Out1* and *Out2*, respectively, as shown in Fig. 4(a).

Fig. 4(b) is an image of the experimental test bed showing a vertically coupled 8-fiber array (FA), a 15-port multi-contact wedge (MCW) DC probe, and the SOI device under test (DUT). The continuous wave (CW) optical input from a tunable C-band laser is polarization controlled, and then coupled to the DUT through surface grating couplers (GCs) of -6.5 dB fiber-to-chip coupling loss per GC. Heater bias voltages are applied from tunable DC power supplies, and the optical output power is measured by a power meter. An ADC based 2-mode multiplexer, shown in Fig. 4(c), is used for multiplexing the TE0 and the TE1 modes. The CW response of the 2-mode multiplexer is first measured. The normalized optical transmission of this mode-multiplexer as a function of wavelength is shown in Fig. 4(d). The broadband mode-multiplexer exhibits -1.8 dB IL and -22.0 dB crosstalk for the TE0 mode, and -2.7 dB IL and -30.8 dB crosstalk for the TE1 mode, respectively within 1520 nm to 1580 nm wavelength range. The lower propagation constant ($\beta = 2\pi n_{eff}/\lambda$) of the TE1 mode due to the lower

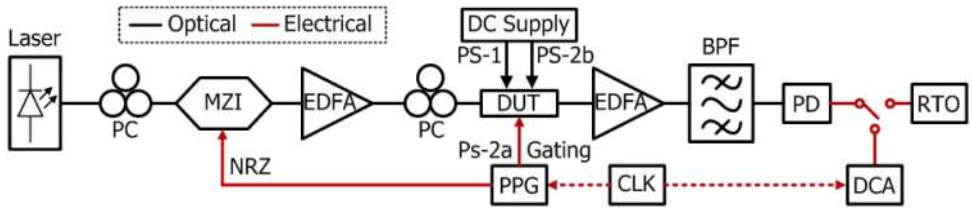

Fig. 5. Experimental setup for the scalable multimode switch (SMS) measurement. The optical and electrical connections are shown as black and red lines, respectively. PC: polarization controller, MZI: Mach-Zehnder interferometer, EDFA: Erbium doped fiber amplifier, DUT: device under test, BPF: band-pass filter, PD: photodetector, RTO: real-time oscilloscope, DCA: digital communication analyzer, CLK: clock synthesizer, PPG: pulse pattern generator, NRZ: non-return-to-zero data signal.

effective refractive index inside the channel waveguide is attributed to the higher IL for the TE1 mode. The electrical resistance of the phase shifter is measured on a 200 μm $\times$ 6 μm heater test structure (Fig. 4(e)), and shown in Fig. 4(f). The measured resistance is 137.5 Ω at room temperature.

For payload data transmission validation, the CW optical input from the laser is modulated by a 10 Gb/s NRZ PRBS31 signal, generated by a pulse pattern generator (PPG), shown in Fig. 5. The modulated and amplified signal is transmitted to the device under test (DUT), and then detected by a 46 GHz off-chip photoreceiver with a responsivity of 0.7 A/W after filtering out any out-of-band noise. The switch responses are recorded in real-time using a 350 MHz real-time oscilloscope (RTO) while recording the eye diagrams using a digital communication analyzer (DCA), which is synchronously triggered with the PPG by a 20 GHz clock synthesizer (CLK). A 18.6 kHz electrical square wave gating signal of 16 ns fall and rise time is applied to the PS-2a phase shifter, with the PS-1 and PS-2b phase shifters biased at fixed voltages to achieve the lowest IL in the transmitting channel.

A. Individual-Mode Switching Experiment

The normalized optical transmissions as a function of wavelength are shown in Fig. 6(a) for the bar state and in Fig. 6(b) for the cross state. In the bar state (Fig. 6(a)), the measured IL at 1550 nm are -2.8 dB for the TE0 input (*TE0-in*) and -6.5 dB for the TE1 input (*TE1-in*). The crosstalks are -16.2 dB and -14.0 dB for the *TE0-in* and the *TE1-in* inputs, respectively. In the cross state (Fig. 6(b)), the ILs in *TE0-in* and *TE1-in* inputs are -2.8 dB and -7.3 dB, respectively; and the crosstalks are -19.2 dB and -19.3 dB, respectively. These values include the IL and crosstalk of the 2-mode multiplexer, reported in Fig. 4(d). As different waveguide modes have different effective indices, and the thermo-optic phase-shift is a function of effective index of the individual modes, the phase-tuning of each mode requires different bias voltage in the heaters. The bias optimization of the PS-2a and the PS-2b phase shifters at 1560 nm from 0 V to 3.5 V are shown in Fig. 6(c) and (d) for the *TE0-in* input and in Fig. 6(e) and (f) for the *TE1-in* input, respectively. As the *TE0-in* input is not affected by the PS-1 phase shifter, this bias is fixed at 0 V. However, a 2.2 V bias is required in the PS-1 phase shifter for the phase matching of two fundamental components of the *TE1-in* input mode. The minimum switching ER for the *TE0-in* and the *TE1-in* inputs are 17.7 dB and 19.2 dB, respectively.

The switching responses for the *TE0-in* and *TE1-in* inputs are shown in Fig. 7(a) and (b), respectively. The *TE0-in* transmission exhibits 9.5 μs rise time and 7.4 μs fall time for the bar state (*TE0*$\rightarrow$*Out1*), and 9.8 μs rise time and 9.6 μs fall time for the cross state (*TE0*$\rightarrow$*Out2*). For the *TE1-in* transmission (Fig. 8(b)), the rise and fall times in the bar state (*TE1*$\rightarrow$*Out2*) are 7.0 μs and 8.3 μs, respectively. In the cross state (*TE1*$\rightarrow$*Out1*), the rise and fall times are 7.4 μs and 9.6 μs, respectively. Dynamic switching responses with payload data transmissions are shown next to each corresponding channel. The corresponding eye diagrams with measured electrical signal-to-noise ratios (SNRs) are shown next to each switching response. Open eyes are observed in all cases confirming the signal integrity with distortion free high-speed data transmission.

B. Dual-Mode Switching Experiment

The operation principle and experimental demonstration of simultaneous dual-mode transmission in an MMI based mode (de)multiplexer is reported in [19]. For the reconfigurable switching of two simultaneous TE modes (*TE0+TE1-in*), the PS-1 phase shifter is optimized so that the combined light beam of the *TE1-in* mode components always appear in the middle output port of MMI-B (Fig. 2(d)), and the power divided light beams from the *TE0-in* mode appear in the upper and the lower input ports. As each output beam is $2\pi/3$ out-of-phase with each other, by ensuring proper phase control using PS-2a and PS-2b phase shifters, dual-mode switching is achieved in the output of MMI-C. Although the ADC based mode multiplexer (Fig. 4(c)) can provide <-20 dB crosstalk over a large wavelength range (1520 nm –1580 nm) for individual-mode switching, the operating range reduces below 12 nm for the dual-mode transmission with a large (>-10 dB) crosstalk. However, the MMI based mode multiplexer, as in [19], provides broadband response and sufficient crosstalk for simultaneous 2-mode switching. For this reason, the dual-mode (*TE0+TE1-in*) characterization is done using a MMI based mode multiplexer followed by the SMS of Fig. 1, with an additional 16.5 mW power consumption due to the phase tuning in the mode multiplexer. As the switching section i.e., SMS is the same in both structures, this modification does not limit the functionality of the SMS for dual-mode switching. Indeed, a design improvement is required for the ADC based mode multiplexer to demonstrate broadband and low crosstalk dual-mode transmission.

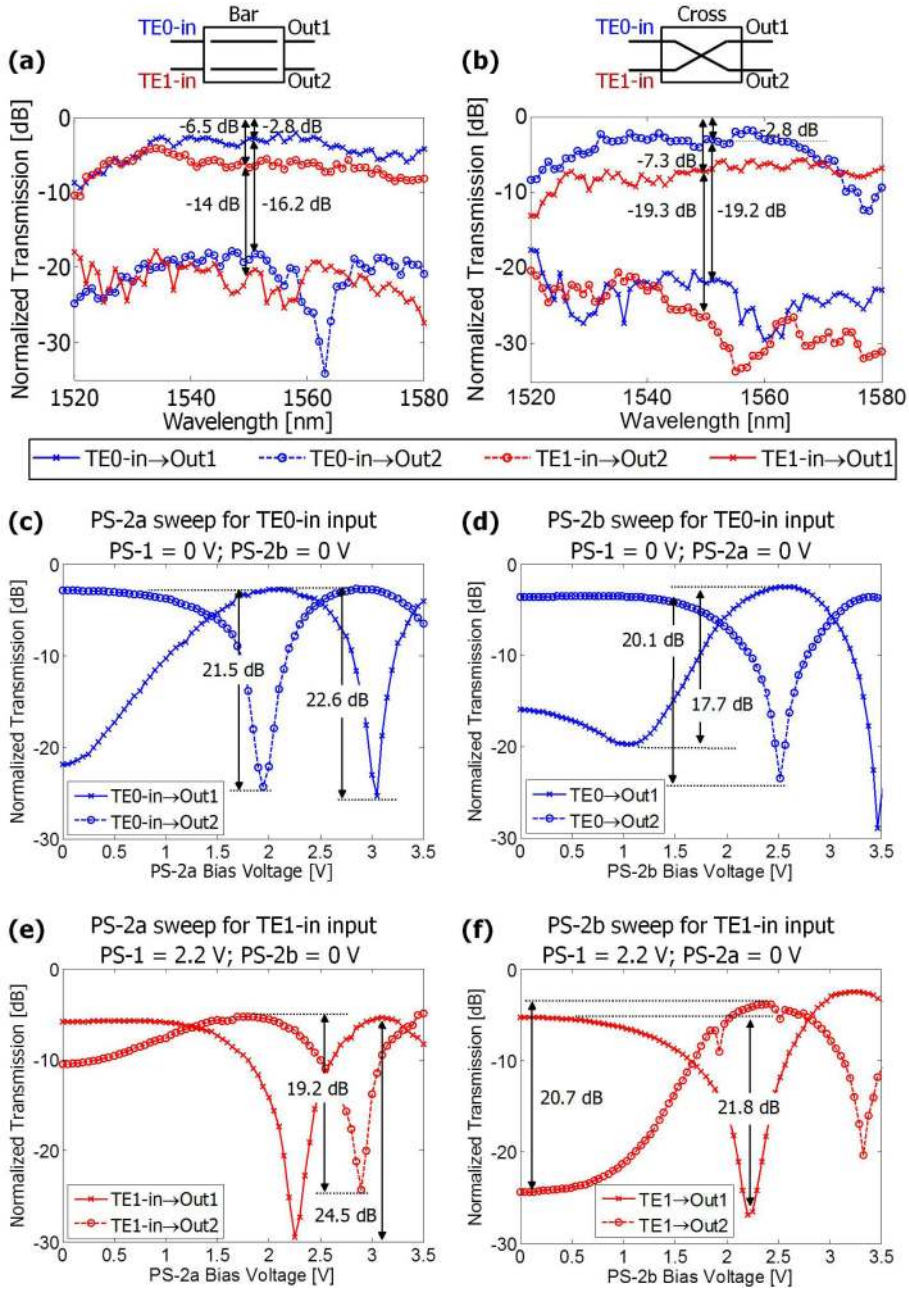

Fig. 6. Normalized individual-mode optical transmissions of the SMS for the *TE0-in* and the *TE1-in* input modes in the (a) bar state and in the (b) cross state as a function of wavelength; (c) and (d) are the normalized transmissions for the *TE0-in* input as a function of PS-2a and PS-2b bias voltages, respectively, from 0 V to 3.5 V when PS-1 = 0 V; (e) and (f) are the normalized transmissions for the *TE1-in* input as a function of PS-2a and PS-2b bias voltages, respectively, from 0 V to 3.5 V when PS-1 = 2.2 V.

Normalized optical transmissions as a function of wavelength from 1520 nm – 1580 nm in dual-mode (*TE0+TE1-in*) is shown in Fig. 8(a) and (b) for *Out1* and *Out2* output ports, respectively. A −7.0 dB IL and −11.9 dB crosstalk are observed in the *Out1* output port, and −6.9 dB IL and −17.5 dB crosstalk are observer in the *Out2* output port. The normalized transmissions of *TE0+TE1-in* input mode as a function of bias voltages of PS-2a and PS-2b phase shifters from 0 V to 4.0 V at 1560 nm are shown in Fig. 8(c) and (d), respectively. The lowest switching ER is 12.0 dB for the *TE0+TE1-in*→*Out2* transmission. The dual-mode switching performances, demonstrating 2 × 10 Gb/s aggregated bandwidth, are shown in Fig. 9(a) and (b) for the *Out1* and the *Out2* output ports, respectively. The slowest rise and fall times, in response to the 18.6 kHz square wave gating signal, are 7.1 μs and 7.6 μs, respectively. The eye height and the electrical SNR decrease than individual-mode switching, which is attributed to the larger IL and crosstalk, observed in Fig. 8(a) and (b). The dynamic switching is shown next to the static switching results. The CW measurement results are summarized in Table I and the switching performances are

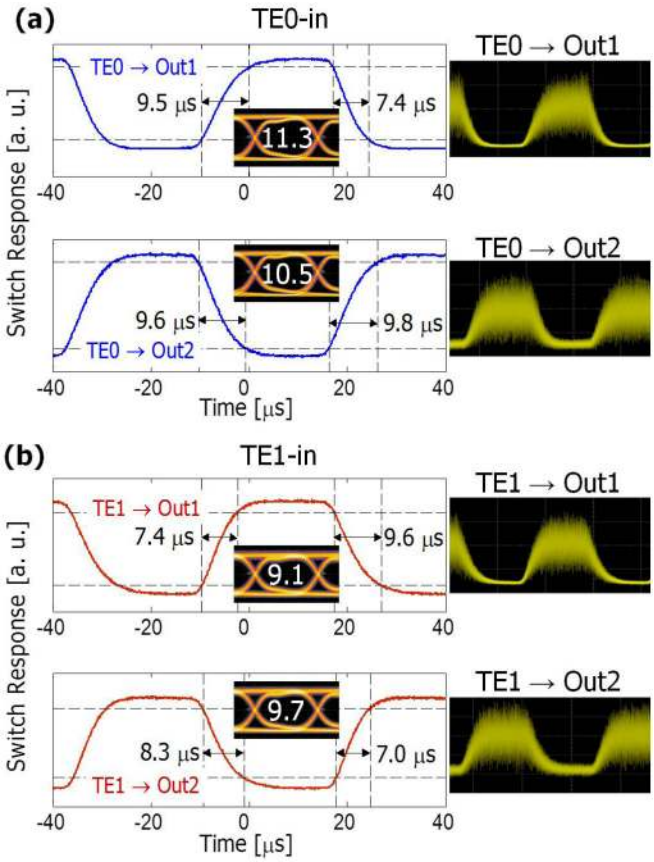

Fig. 7. Measured on-off-keying switching of the MSS for the (a) *TE0-in*, and (b) *TE1-in* input modes at 1560 nm, showing the static (left) and the dynamic (right) responses in individual-mode transmission. Insets of the static responses show the measured eye diagrams with the electrical SNRs.

TABLE I
INSERTION LOSS (IL), CROSSTALK AND AVERAGE HEATER POWER CONSUMPTION IN THE 2-MODE SMS WITHIN 1520 NM AND 1580 NM WAVELENGTH RANGE

Input	Output	IL (-dB)	Crosstalk (-dB)	Heater Power (mW)
TE0	Bar	2.0↔9.3	13.3↔30.7	48.3
	Cross	1.7↔12.3	9.2↔26.3	0
TE1	Bar	4.2↔10.5	7.5↔19.6	84.9
	Cross	5.6↔13.0	7.3↔27.0	126.3
TE0+TE1	Out1	5.3↔8.5	8.1↔20.6	98.2
	Out2	3.8↔9.7	8.9↔19.8	134.7

summarized in Table II for *TE0-in*, *TE1-in* and *TE0+TE1-in* input modes.

IV. DISCUSSION

The SMS can be scaled up to switch higher order TE modes (e.g., TE3 and TE4) by carefully optimizing the width and the length of the mode decomposer MMI (MMI-A) with additional output ports followed by the necessary phase shifters. However, the higher order modes will increase both the IL and the power

TABLE II
SWITCHING PERFORMANCES FOR TE0, TE1 AND TE0+TE1 INPUT MODES AT 1560 NM

	Switching ER (dB)	Rise Time (μs)	Fall Time (μs)	Electrical SNR
TE0→Out1	17.7	9.5	7.4	11.0
TE0→Out2	20.1	9.8	9.6	10.5
TE1→Out1	21.8	7.4	9.6	9.1
TE1→Out2	19.2	7.0	8.3	9.7
TE0+TE1→Out1	5.0	7.6	8.3	7.6
TE0+TE1→Out2	7.1	5.1	8.3	6.3

consumption somewhat challenging its scalability. For example, the estimated IL and power consumption for the TE3 input mode in a similar 4-mode switch, calculated using numerical approximation, is −8.2 dB and 128 mW, respectively. In the proposed 4-mode SMS, as shown in Fig. 10(a), a 1 × 3 mode separator MMI of 7 μm width and 145.6 μm length reproduces the even TE0 and TE2 modes to its middle output port. The odd modes (i.e. TE1 and TE3) are divided into two lower order mode components, and then mapped to the upper and the lower output ports. The TE1 mode is decomposed to TE0 components, and the TE3 mode is decomposed to TE1 components [24]. These decomposed mode components are phase-tuned and demultiplexed in the 2-mode (de)multiplexer [19]. The demultiplexed modes are recombined in the 3 dB coupler stage followed by a 4 × 4 switching stage consisting of a 4 × 4 MMI and four phase shifters. There are eight phase shifters in this structure: each 2-mode switch has two phase shifters and the switching stage has four phase shifters. The electric fields in the mode separator MMI for the first four TE mode inputs are shown in Fig. 10(b), demonstrating the capability of simultaneous 4-mode transmission.

To study the scalability of the SMS, the 2-mode switch is compared with a mode selecting switch (MSS) allowing either the TE0 or TE1 mode transmission enabling a single-mode switch, reported in [16]. As this MSS utilizes the same mode decomposer, cascaded MMI couplers and metal Ti/N phase shifter of similar phase tuning efficiency, the comparison is consistent and reasonable. The IL and power consumption of the proposed 3-mode switch, as shown in Fig. 1, is also considered in the scalability comparison. The measured average IL and average heater power for the mode selecting single-mode switch are previously reported to be −1.95 dB and 23.3 mW, respectively in [16]. The experimentally mesured average IL and average heater power for the 2-mode SMS for the individual-mode operation (i.e. *TE1-in* and *TE1-in*) are −6.8 dB and 65.0 mW, respectively in an ADC based SMS (see Table I). As the dual-mode switching using ADC based mode multiplexer requires further optimization, this is not considered in the scalability study in Fig. 11(a) and (b). An initial characterization of the 3-mode switch demonstrates an average IL of −7.0 dB and an average heater power of 91.8 mW for the individual-mode transmission. These values are plotted in Fig. 11(a) and (b) as a function of the number of TE modes. In a 2 × 2 MMI based single-mode MZI switch matrix, the overall

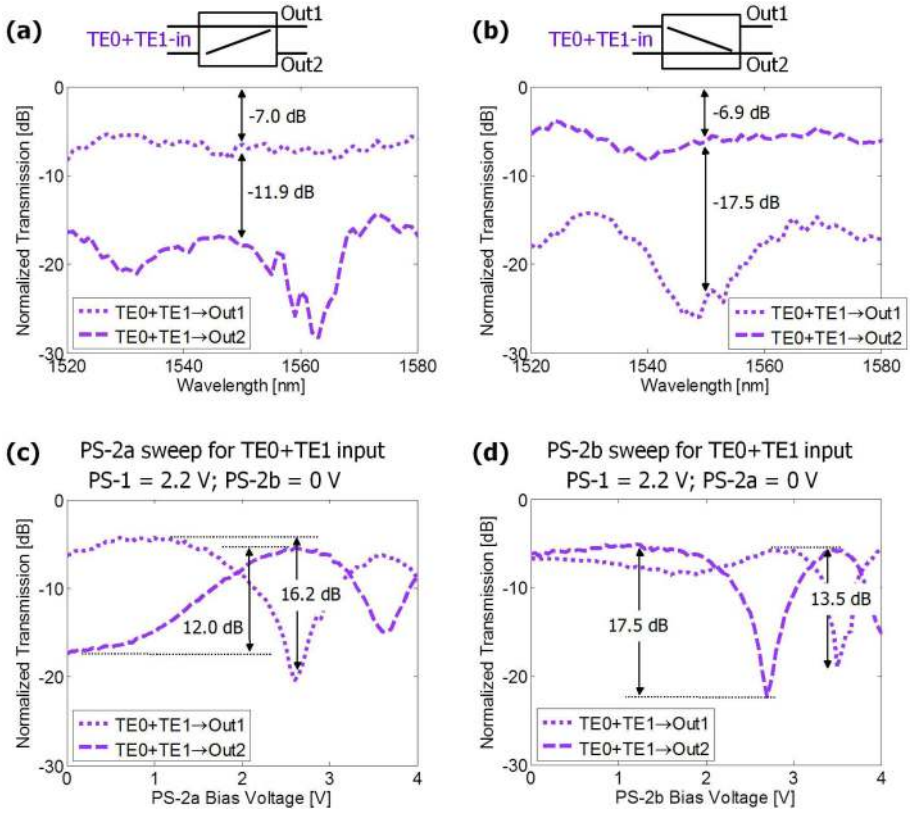

Fig. 8. Normalized dual-mode optical transmissions of the SMS for the *TE0+TE1-in* input mode for the (a) *Out1* and the (b) *Out2* output ports as a function of wavelength; (c) and (d) are the normalized transmissions for *TE0+TE1-in* input as a function of PS-2a and PS-2b bias voltages, respectively, from 0 V to 4.0 V when PS-1 = 2.2 V.

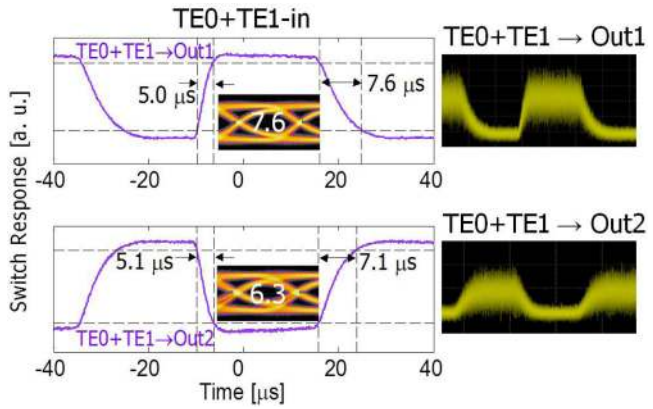

Fig. 9. Measured on-off-keying switching of the MSS for the *TE0+TE1-in* input mode at 1560 nm, showing the static (left) and the dynamic (right) responses. Insets of the static responses show the measured eye diagrams with the electrical SNRs.

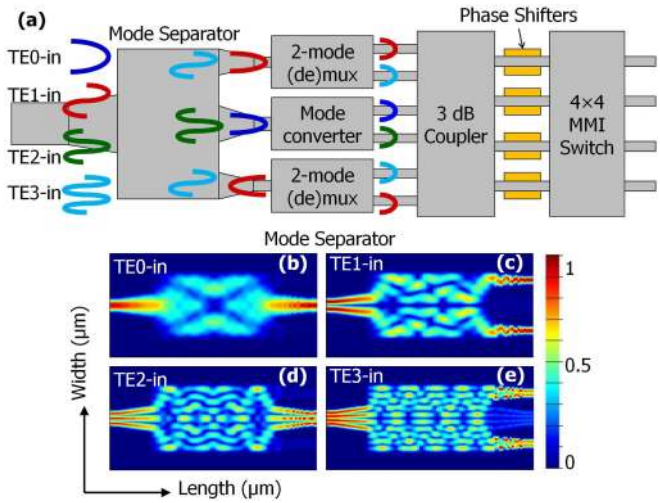

Fig. 10. (a) Schematic block diagram of the 4-mode SMS for the switching of first four TE modes, i.e. TE0, TE1, TE2 and TE3; the simulated electric fields in the mode separator MMI are shown underneath for (b) *TE0-in*; (c) *TE1-in*; (d) *TE2-in*; and (e) *TE3-in* input modes.

IL from an input port to an output port can be estimated by simply adding up the ILs of each MMI along the I/O path, as each MMI is identically designed exhibiting similar IL and crosstalk. However, in a multimode SMS, the dimensions of the MMIs, and the number of cascading stages change as the number of mode increases. Thus simulating the IL of a single MMI and adding it up for higher order mode switching is not an acceptable method.

In Fig. 11(a), the IL of each MMI is estimated by EME simulation, and the S-parameters are extracted to build a circuit model in Lumerical' s Interconnect [29]. The calculated ILs from this circuit level simulation are plotted in Fig. 11(a) (blue dashed

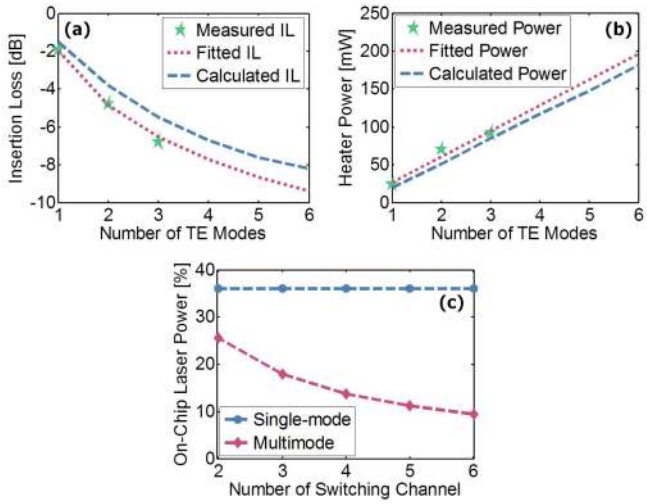

Fig. 11. Measured (green star), fitted (pink dotted line) and simulated (blue dashed line) (a) insertion loss, and (b) average heater power in the SMS as a function of number of propagating modes; (c) is the on-chip power fraction (%) of lasers with respect to total on-chip power in the single-mode (blue line) and the multimode (pink line) switches; the power consumption is calculated from the extrapolated heater powers from (b).

line), along with the measured (green star) and fitted (pink dotted line) values. The higher ILs in the measured and the fitted plots than the simulated one is attributed to the higher scattering loss and wavelength sensitivity in the fabricated device, an impact of fabrication non-uniformity. The power consumption per phase shifter is estimated through simulation, as reported in [30]. Based on the number of phase shifter used in the 2-mode and the 3-mode switches, we estimate the number of phase shifter required for higher order modes, and calculate the total heater power from simulation. The calculated average heater powers are plotted in Fig. 11(b), along with the fitted and measured values. The calculated and fitted powers are in good agreement. The slight variation arises from the uniform power increment in the calculated plot versus the change in heater power consumption for different phase shifters in the fabricated device. A -9.0 dB average IL and 163.0 mW average heater power is expected for a multimode switch capable of switching five TE modes. The heater power budget can be further improved by using resistive type doped silicon phase shifter [31] of 21 mW/π-shift, calculated in [30] replacing the metal heater of 35.5 mW/π-shift, as measured in [16]. Using this resistive phase shifter, we achieved an on-chip energy efficiency of 1.55 pJ/bit, including the laser power, and a 2×10 Gb/s aggregated bandwidth in an RMDS based MDM photonics link [19]. As the same RMDS (MMI-A) can decompose TE0, TE1 and TE2 modes, a single device is required for the 2-mode switch and the 3-mode switch without increasing the footprint.

As most of the power consumption of an integrated photonic switch is caused by the power of the laser [32], it is essential to evaluate an integrated switch in term of the on-chip laser power. The heater powers from Fig. 11(b) are used to calculate the on-chip power fraction (%) of the laser for single-mode and multimode switches of two to six switching channels, as shown in Fig. 11(c). A 2×2 MZI switch test structure with 2×2 MMI couplers and the same Ti/W metal heater phase shifter (as used in the SMS) is characterized as a single-mode 2-channel crossbar switch. The measured average switching power of this 2×2 MZI switch is 40 mW. In the total on-chip power consumption of a switching channel, a 66 mW power of a 10 Gb/s directly modulated tunable on-chip VCSEL is included [33]. The on-chip power of a hybrid-integrated 40 Gb/s photoreceiver including a Ge-on-Si photodetector and a wire-bonded transimpedance amplifier (TIA) is reported to be 77 mW [34]. As the single-mode switching requires individual laser per switching channel, the ratio of laser power to the total on-chip power remains constant (38.06%) regardless of the number of channels. On the other hand, a 3-channel multimode switch, for example, needs only one VCSEL providing equal optical power to each channel (3 mW optical output power). The power consumption by the laser for three-mode transmission is 79.7 mW including the 66 mW electrical driving power and 13.7 mW additional power to account for the higher optical output [35]. The laser wall-plug efficiency is not taken into account, as done in [32]. The receiver power and the heater power remain the same as the 3-channel single-mode switch. This estimates a laser power fraction of 19.8% in the 3-channel multimode switch, which is almost half the laser power fraction of a 3-channel single-mode switch of 36.06%. This allows large reduction in total on-chip power consumption in the multimode switch by saving approximately 27% energy in 2-channel switch up to 63% energy in the 6-channel switch compared to the corresponding single-mode switches. Thus, the proposed SMS can be used in the deployment of energy-efficient switch matrix in mode-division multiplexed integrated photonics systems. Indeed, the on-chip loss budget and the photodetector sensitivity have to be considered in this estimation, which needs detail investigation of power consumption analysis.

V. Conclusion

To summarize, we demonstrate a novel scalable multimode switch (SMS) using multimode interference couplers and Ti/W metal heater phase shifters for reconfigurable MDM silicon photonic systems. To the best of our knowledge, this is the first demonstration of a SOI MDM switch that allows path-reconfigurable switching between first two (TE0 and TE1) or three (TE0, TE1 and TE2) TE modes using the same device, which can significantly improve the bandwidth density and power consumption. The 2-mode SMS exhibits <-14 dB crosstalk and <-7.3 dB IL in the individual-mode switching, and <-11.9 dB crosstalk and <-7.0 dB IL in the simultaneous dual-mode switching at 1550 nm. The measured switching ER is greater than 19.2 dB and 12.0 dB for individual-mode and dual-mode, respectively. Open and clear eye diagrams for all data channels demonstrate distortion-free data transmission with an aggregated bandwidth of 2×10 Gb/s. The slowest switching times are <9.8 μs for the *TE0-in* input, <9.7 μs for the *TE1-in* input, and <7.6 μs for *TE0+TE1-in* input modes. The SMS can be scaled up for higher order mode switching by engineering the length and the width of the MMI couplers with more output ports and phase shifter stages. The power consumption analysis

demonstrates the higher energy efficiency of the SMS than a single-mode MZI switch. The SMS can be a viable solution for the deployment of high-throughput energy-efficient photonics switching in silicon MDM interconnects.

REFERENCES

[1] Cisco Systems, Inc., "Cisco global cloud index: Forecast and methodology, 2016–2021," White Paper, 2017.

[2] M. D. Avgerinou, P. Bertoldi, and L. Castellazzi, "Trends in data centre energy consumption under the European Code of conduct for data centre energy efficiency," *Energies*, vol. 10, no. 10, Sep. 2017, Art. no. 1470.

[3] W. Dargie, D. Schoeniger, L. Szilagyi, X. An, R. Henker, and F. Ellinger, "A highly adaptive and energy-efficient optical interconnect for on-board server communications," in *Proc. 26th Int. Conf. Comput. Commun. Netw.*, Jul. 2017, pp. 1–8.

[4] C. A. Thraskias *et al.*, "Survey of photonic and plasmonic interconnect technologies for intra-data center and high-performance computing communications," *IEEE Commun. Surveys Tuts.*, vol. 20, no. 4, pp. 2758–2783, Fourth Quarter 2018.

[5] D. A. B. Miller, "Attojoule optoelectronics for low-energy information processing and communications," *J. Lightw. Technol.*, vol. 35, no. 3, pp. 346–396, Feb. 2017.

[6] H. D. Thacker *et al.*, "An all-solid-state, WDM silicon photonic digital link for chip-to-chip communications," *Opt. Express*, vol. 23, no. 10, pp. 12808–12822, May 2015.

[7] A. L. Lentine and C. T. DeRose, "Challenges in the implementation of dense wavelength division multiplexed (DWDM) optical interconnects using resonant silicon photonics," *Proc. SPIE*, vol. 9772, 2016, Art. no. 977207.

[8] J. Wang, S. Chen, and D. Dai, "Silicon hybrid demultiplexer with 64 channels for wavelength/mode-division multiplexed on-chip optical interconnects," *Opt. Lett.*, vol. 39, no. 24, pp. 6993–6996, Dec. 2014.

[9] M. Ye, Y. Yu, J. Zou, W. Yang, and X. Zhang, "On-chip multiplexing conversion between wavelength division multiplexing–polarization division multiplexing and wavelength division multiplexing–mode division multiplexing," *Opt. Lett.*, vol. 39, no. 4, pp. 758–761, Feb. 2014.

[10] C. Li, D. Liu, and D. Dai, "Multimode silicon photonics," *Nanophotonics*, vol. 8, pp. 227–247, 2018.

[11] D. Dai, J. Wang, and S. He, "Silicon multimode photonic integrated devices for on-chip mode-division-multiplexed optical interconnects (invited review)," *Progr. Electromagn. Res.*, vol. 143, pp. 773–819, Dec. 2013.

[12] L. Yang *et al.*, "General architectures for on-chip optical space and mode switching," *Optica*, vol. 5, no. 2, pp. 180–187, Feb. 2018.

[13] M. Ye, Y. Yu, C. Sun, and X. Zhang, "On-chip data exchange for mode division multiplexed signals," *Opt. Express*, vol. 24, no. 1, pp. 528–535, Jan. 2016.

[14] X. Zi, L. Wang, K. Chen, and K. S. Chiang, "Mode-selective switch based on thermo-optic asymmetric directional coupler," *IEEE Photon. Technol. Lett.*, vol. 30, no. 7, pp. 618–621, Apr. 2018.

[15] Q. Huang, W. Jin, and K. S. Chiang, "Broadband mode switch based on a three-dimensional waveguide Mach-Zehnder interferometer," *Opt. Lett.*, vol. 42, no. 23, pp. 4877–4880, Dec. 2017.

[16] R. B. Priti, H. P. Bazargani, Y. Xiong, and O. Liboiron-Ladouceur, "Mode selecting switch using multimode interference for on-chip optical interconnects," *Opt. Lett.*, vol. 42, no. 20, pp. 4131–4134, Oct. 2017.

[17] R. B. Priti, F. Shokraneh, and O. Liboiron-Ladouceur, "Scalable 2×2 multimode switch for mode-multiplexed silicon photonics interconnects," in *Proc. Asia Commun. Photon. Conf.*, Oct. 2018, pp. 1–8.

[18] R. B. Priti, G. Zhang, and O. Liboiron-Ladouceur, "3×10 Gb/s silicon three-mode switch with 120° hybrid based unbalanced Mach-Zehnder interferometer," *Opt. Express*, no. 10, pp. 14199–14212, May 2019.

[19] R. B. Priti and O. Liboiron-Ladouceur, "A reconfigurable multimode demultiplexer/switch for mode-multiplexed silicon photonics interconnects," *IEEE J. Sel. Topics Quantum Electron.*, vol. 24, no. 6, Nov./Dec. 2018, Art. no. 8300810.

[20] P. J. Reyes-Iglesias, I. Molina-Fernández, A. Moscoso-Mártir, and A. Ortega-Moñux, "High-performance monolithically integrated 120° downconverter with relaxed hardware constraints," *Opt. Express*, vol. 20, no. 5, pp. 5725–5741, Feb. 2012.

[21] K. Solehmainen, M. Kapulainen, M. Harjanne, and T. Aalto, "Adiabatic and multimode interference couplers on silicon-on-insulator," *IEEE Photon. Technol. Lett.*, vol. 18, no. 21, pp. 2287–2289, Nov. 2006.

[22] L. B. Soldano and E. C. M. Pennings, "Optical multi-mode interference devices based on self-imaging: Principles and applications," *J. Lightw. Technol.*, vol. 13, no. 4, pp. 615–627, Apr. 1995.

[23] D. Chen, X. Xiao, L. Wang, Y. Yu, W. Liu, and Q. Yang, "Low-loss and fabrication tolerant silicon mode-order converters based on novel compact tapers," *Opt. Express*, vol. 23, no. 9, pp. 11152–11159, May 2015.

[24] Y. Kawaguchi and K. Tsutsumi, "Mode multiplexing and demultiplexing devices using multimode interference couplers," *Electron. Lett.*, vol. 38, no. 25, pp. 1701–1702, Dec. 2002.

[25] J. D. Love and N. Riesen, "Single-, few-, and multimode y-junctions," *J. Lightw. Technol.*, vol. 30, no. 3, pp. 304–309, Feb. 2012.

[26] M. Teng, K. Kojima, T. Koike-Akino, B. Wang, C. Lin, and K. Parsons, "Broadband SOI mode order converter based on topology optimization," in *Proc. Opt. Fiber Commun. Conf. Expo.*, Mar. 2018, Paper Th2A.8.

[27] J. Qiu, D. Zhang, Y. Tian, J. Wu, Y. Li, and Y. Wang, "Performance analysis of a broadband second-order mode converter based on multimode interference coupler and phase shifter," *IEEE Photon. J.*, vol. 7, no. 5, Oct. 2015, Art. no. 7102908.

[28] NanoSOI fabrication process. [Online]. Available: http://www.appliednt.com/nanosoi. Accessed on: Apr. 29, 2019.

[29] MMI coupler. [Online]. Available: https://www.lumerical.com/. accessed: Apr. 29, 2019.

[30] R. B. Priti, Y. Xiong, and O. Liboiron-Ladouceur, "Efficiency improvement of an O-band SOI-MZI thermo-optic matrix switch," in *Proc. IEEE Photon. Conf.*, Oct. 2016, pp. 823–824.

[31] M. R. Watts, J. Sun, C. DeRose, D. C. Trotter, R. W. Young, and G. N. Nielson, "Adiabatic thermo-optic Mach-Zehnder switch," *Opt. Lett.*, vol. 38, no. 5, pp. 733–735, Mar. 2013.

[32] A. V. Krishnamoorthy, H. Schwetman, X. Zheng, and R. Ho, "Energy-efficient photonics in future high-connectivity computing systems," *J. Lightw. Technol.*, vol. 33, no. 4, pp. 889–900, Feb. 2015.

[33] S. Paul *et al.*, "10-Gb/s direct modulation of widely tunable 1550-nm MEMS VCSEL," *IEEE J. Sel. Topics Quantum Electron.*, vol. 21, no. 6, pp. 436–443, Nov. 2015.

[34] Z. Xuan, R. Ding, Y. Liu, T. Baehr-Jones, M. Hochberg, and F. Aflatouni, "A low-power hybrid-integrated 40-Gb/s optical receiver in silicon," *IEEE Trans. Microw. Theory Techn.*, vol. 66, no. 1, pp. 589–595, Jan. 2018.

[35] W. Hamad, M. B. Sanayeh, T. Siepelmeyer, H. Hamad, and W. H. E. Hofmann, "Small-signal analysis of high-performance VCSELs," *IEEE Photon. J.*, vol. 11, no. 2, Apr. 2019, Art. no. 1501212.

Rubana Bahar Priti (S'14) received the B.Sc. and M.S. degrees in applied physics, electronics and communication engineering from the University of Dhaka, Dhaka, Bangladesh, and a second M.S. degree in electrical engineering from South Dakota State University, Brookings, SD, USA, in 2013. She is currently working toward the Ph.D. degree in electrical engineering with McGill University, Montreal, QC, Canada, specializing on energy-efficient silicon photonics interconnects. Her research interests include silicon-integrated photonics and photonic-electronic co-packaging. She is a recipient of the McGill Engineering Doctoral Award, the NSERC SiEPIC doctoral scholarship, and the IEEE Photonics Society WIP Travel Grant.

Odile Liboiron-Ladouceur (M'95–SM'14) received the B.Eng. degree in electrical engineering from McGill University, Montreal, QC, Canada, in 1999, and the M.S. and Ph.D. degrees in electrical engineering from Columbia University, New York, NY, USA, in 2003 and 2007, respectively. She is currently an Associate Professor and Canada Research Chair in Photonics Interconnect with the Department of Electrical and Computer Engineering, McGill University. She holds six issued U.S. patents and coauthored more than 55 peer-reviewed journal papers and more than 100 papers in conference proceedings. Her research interests include optical systems, photonic-integrated circuits, and photonic interconnects. She is the 2018 recipient of McGill Principal's Prize for Outstanding Emerging Researcher.